


Article

Spinel rGO Wrapped CoV_2O_4 Nanocomposite as a Novel Anode Material for Sodium-Ion Batteries

Rasu Muruganantham , Jeng-Shin Lu and Wei-Ren Liu *

Department of Chemical Engineering, R&D Center for Membrane Technology, Research Center for Circular Economy, Chung Yuan Christian University, Taoyuan City 32023, Taiwan; murugaphd@yahoo.com (R.M.); gto42916@gmail.com (J.-S.L.)

* Correspondence: wrliu@cycu.edu.tw; Tel.: +886-3-2654140; Fax: +886-3-2654199

Received: 18 February 2020; Accepted: 1 March 2020; Published: 3 March 2020



Abstract: Binary mixed transition-based metal oxides have some of the most potential as anode materials for rechargeable advanced battery systems due to their high theoretical capacity and tremendous electrochemical performance. Nonetheless, binary metal oxides still endure low electronic conductivity and huge volume expansion during the charge/discharge processes. In this study, we synthesized a reduced graphene oxide (rGO)-wrapped CoV_2O_4 material as the anode for sodium ion batteries. The X-ray diffraction analyses revealed pure-phased CoV_2O_4 (CVO) rGO-wrapped CoV_2O_4 (CVO/rGO) nanoparticles. The capacity retention of the CVO/rGO composite anode demonstrated 81.6% at the current density of 200 mA/g for more than 1000 cycles, which was better than that of the bare one of only 73.5% retention. The as-synthesized CVO/rGO exhibited remarkable cyclic stability and rate capability. The reaction mechanism of the CoV_2O_4 anode with sodium ions was firstly studied in terms of cyclic voltammetry (CV) and ex situ XRD analyses. These results articulated the manner of utilizing the graphene oxide-coated spinel-based novel anode- CoV_2O_4 as a potential anode for sodium ion batteries.

Keywords: anode; sodium ion batteries; spinel; reduced graphene oxides

1. Introduction

Energy storage devices, namely batteries, play a cardinal role in the up-to-date development of portable smart technology to heavy electric energy storage devices [1]. Currently, sodium ion batteries (SIBs) display their unique advantages of abundant Na resources, being economically low cost, and having a similar device strategy as the viable lithium ion batteries [2,3]. However, the developments of appropriate electrode materials are some of the major critical topics for SIBs since the larger ionic radius of Na hinders the electrochemical reaction via graphite as the anode for Na ion storage. Currently, metal-based electrode materials, such as metal oxides [4], metallic selenides [5], bimetallic sulfides [6], and other metal-based electrode materials [7–9], have been widely established and developed for high-energy density SIBs applications. Among these, vanadium with mixed metal oxide-based anode materials tends to display improved electrochemical properties because of the higher energy density, existing in a diversity of oxidation states, and offering a considerably wider potential window for Li/Na ion batteries [8–11]. Nonetheless, vanadate-based anodes for SIBs suffer from rapid capacity decay and poor rate performance as a result of the extreme pulverization and slow kinetics upon the sodiation/desodiation process [11]. These drawbacks have been amended by modified carbonaceous materials.

Graphene is deliberated as a supreme support due to its enormous specific surface area, high mechanical strength, and superior electronic conductivity. Wang et al. [12] described reduced graphene oxide (rGO) as an anode material for SIBs, and it exhibited a reversible capacity of

174.3 mAh g⁻¹ at 0.2 C (40 mA g⁻¹) over 250 cycles. Wen et al. reported a reversible capacity of 280 mAh g⁻¹ at a current density of 20 mA g⁻¹ through increasing the interlayer spacing to 4.3 Å [13]. Kumar et al. recently observed that the rGO anode delivered a discharge capacity of 272 mA h g⁻¹ at a current density of 50 mA g⁻¹ [14]. Thus, the results indicated rGO as a potential electrochemically active material for SIBs. Recently, several researchers have focused on rGO-modified mixed metal oxide-based anode materials for high-rate and long-cycle Na ion storage applications. Wu et al. [15] observed the highest reversible capacity of the NiFe₂O₄/rGO(20 wt. %) anode for sodium ion batteries, and the result showed 450 mAh g⁻¹ at 50 mA g⁻¹ after 50 cycles with good cycling stability. Sekhar et al. [16] reported ZnMn₂O₄ with modification of N-doped graphene composite anode materials for Na ion storage. The reversible capacity was found to be 170 mAh g⁻¹ at 100 mA g⁻¹ over the 1000 cycles. Zhang et al. [17,18] reported the Co_{1.8}V_{1.2}O₄/rGO and Mn_{2.1}V_{0.9}O₄/rGO materials for Li ion batteries. Li et al. [19] proposed monodispersed graphene nanosheets on a SnO₂ nanoparticle hybrid electrode material for Li/Na ion batteries. The Na ion storage cell exhibited a high reversible capacity of 314 mAh g⁻¹ at 100 mA g⁻¹ and showed a stable long-term cycling stability with a capacity retention of 77% after 500 cycles. In our previous work, we reported CoV₂O₄ as an anode material for Li ion storage for the first time, and it achieved higher electrochemical performance via carboxymethyl cellulose (CMC) with styrene butadiene rubber (SBR) polymer binder comparable to the conventional PVDF binder [20]. So far, there is no literature available based on CoV₂O₄ or rGO-modified CoV₂O₄ material for sodium ion battery anodes.

In this work, we demonstrate a facile technique to synthesize rGO-wrapped CoV₂O₄ (CVO/rGO) nanocomposite for the first time with a sodium ion storage anode material. The as-prepared materials' thermal stability, crystal phase structure, and surface morphology are evaluated by TG analysis, XRD, microscopy, and BET analysis. The CVO/rGO sample has high thermal stability, a higher specific surface area, and mesoporous nature. TEM result shows that rGO completely encloses the CVO nanoparticles. The resultant CVO/rGO nanocomposite exhibits higher rate performance and excellent long-term cycling stability. The electrochemical kinetic behavior and storage mechanism are proposed via AC impedance, cyclic voltammetry, and ex situ XRD analyses.

2. Experimental Section

2.1. Preparation of rGO-Wrapped CoV₂O₄ Material

All the reagent chemicals were used in the experiment without any further purification of the process. First, 5 wt. % of graphene oxide (GO) was dispersed into 40 mL of methanol (CH₃OH, 99.9%, TEDIA) solution using an ultrasonication process (amplitude of 50 Hz at 30 min). The obtained solution was noted as Solution A. Afterwards, 0.8731 g of cobalt nitrate hexahydrate (Co(NO₃)₂·6H₂O, 98%, SHOWA) and 0.7019 g of ammonium vanadate (NH₄(VO₃), 99%, Alfa Aesar, 99%) were mixed into Solution A and stirred vigorously for 30 min. Then, an equal ratio of 2.5 mL of nitric acid (HNO₃, 69.5%, Scharlau) and 2.5 mL of hydrogen peroxide (H₂O₂, 35%, SHOWA) was dropwise added into the metal and GO mixed solution and stirred for 1 h. The completely mixed solution was transferred into a 100 mL Teflon-lined stainless steel autoclave and reacted in an oven at 200 °C for 3 days, then naturally cooled to room temperature. The precipitate was washed with ethanol several times and dried at 80 °C. Finally, the as-prepared material was calcined at 500 °C for 8 h in a H₂/N₂ atmosphere, and rGO-wrapped CoV₂O₄ (CVO/rGO) with a spinel crystal phase structure was obtained. Bare CoV₂O₄ (CVO) was synthesized by a similar procedure of the abovesaid steps only without GO in the solution. Figure 1a shows the schematic representation of the rGO-wrapped CoV₂O₄ material's preparation.

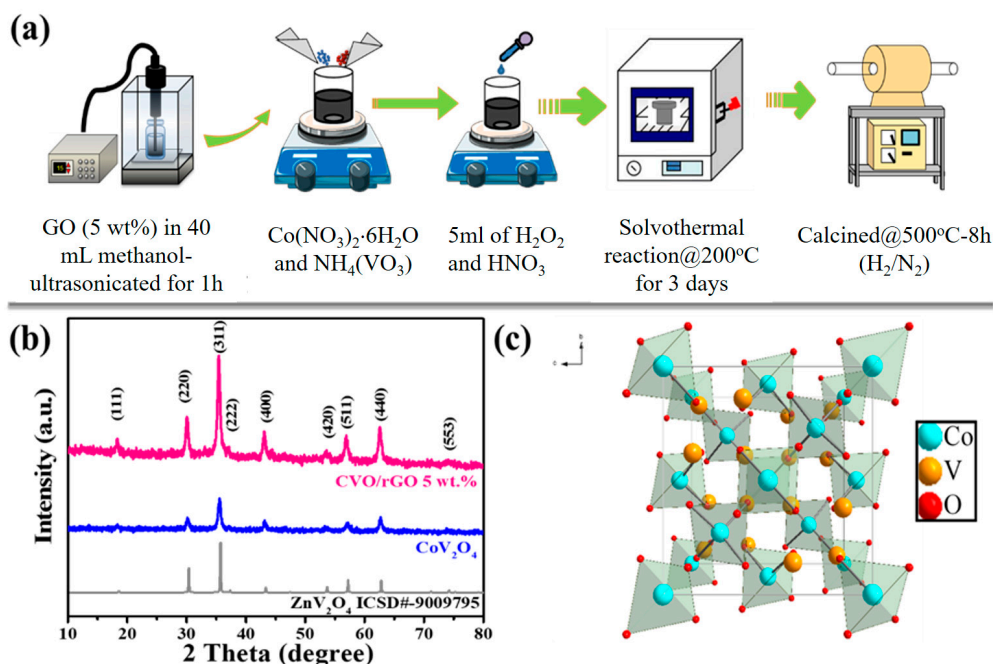


Figure 1. (a) Schematic illustration of the synthesis route for reduced graphene oxide (rGO)-wrapped CoV_2O_4 material; (b) XRD patterns of bare CoV_2O_4 and rGO-wrapped CoV_2O_4 materials; and (c) schematic crystal structure of spinel CoV_2O_4 .

2.2. Characterizations

The thermal behaviors of the as-prepared materials were investigated using TGA analysis. The ramp rate was maintained at $5^\circ\text{C}/\text{min}$ under an air atmosphere. The crystal phase structure and purity were determined by XRD analysis using a D8 diffractometer (Bruker®) with monochromatic $\text{CuK}\alpha$ radiation. The operating voltage, current, and wavelength (λ) were 40 kV, 30 mA, and 1.54060 \AA , respectively. Diffraction data were recorded in the range (2θ) of 10° – 80° . The morphological natures of the as-prepared samples were observed using SEM (Hitachi S-4100) with electron mapping (EDS, X-MAX) and high-resolution TEM (JEM2100) techniques. The specific surface area and porosity were estimated by using A Tristar 3000 accelerated surface area and porosimetry instrument via the N_2 adsorption/desorption isotherm route.

2.3. Preparation of the Electrode Using Cellulose-Based Polymer Binder

The working electrodes were prepared by mixing 80 wt. % of active material (CVO or CVO/rGO), 10 wt. % of conductive additive (Super P, Timcal®), and a 10 wt. % mixture of carboxymethyl cellulose (CMC, 6 wt. %)/styrene butadiene rubber (SBR, 4 wt. %) binder. The CMC/SBR mixture was dissolved in deionized H_2O . Then, the slurry was uniformly coated on a copper foil. The coated Cu foil was dried at 120°C for 6 h using an oven. Finally, it was punched into a disc-like electrode with a diameter of 1.2 cm, 1.5 – 2.0 mg cm^{-2} of active material mass loading, and $\sim 40 \text{ \mu m}$ in thickness.

2.4. Fabrication of the Sodium Ion Cell

The sodium ion storage cell was fabricated using the CR2032 coin-type half cell with sodium metal as the reference electrode and the prepared electrode as the working electrode. Glass fiber (Type A/E, P/N 61630, Pall Corporation) was used as a separator between the working electrode and sodium metal. The electrolyte was composed of 1 M NaClO_4 (99.99%, Sigma-Aldrich, St. Louis, MO, USA) dissolved in a mixture of ethylene carbonate (EC) and diethyl carbonate (DEC) (3:7 *v/v*) with 5 wt. % of fluoroethylene carbonate (FEC). The coin cell assembling procedures were performed using Ar filled glove box (MBraun lab star model) by keeping both the O_2 and H_2O levels less than 1 ppm.

2.5. Electrochemical Measurements

The galvanostatic discharge-charge measurements were performed using a constant current and constant voltage programmable AcuTech battery testing system (New Taipei City, Taiwan, Model 750B) in the potential window of 0.01–3.0 V (V vs. Na/Na⁺) under a 20 ± 2 °C temperature at various rates. The cyclic voltammograms (CV) were measured by the electrochemical workstation of the CH Instruments Analyzer (CHI 6273E, Austin, TX, USA) at a scan rate of 0.5 mV/s in the potential range of 0.001–3.0 V. The AC impedance was carried out in the range of 0.001 Hz–100 kHz at an AC voltage with a 5 mV amplitude.

3. Results and Discussion

A schematic view of the simple preparation of the proposed rGO-wrapped CVO (CVO/rGO) is shown in Figure 1a. The as-synthesized CVO/rGO and bare CVO materials crystal phase structure of the XRD patterns are presented in Figure 1b. As exposed in the diffraction peaks (2θ), values of 18.81°, 31.21°, 36.81°, 38.51°, 44.81°, 55.71°, 59.41°, 65.31°, and 72.31° corresponded to the diffraction planes (111), (220), (311), (222), (400), (420), (511), (440), and (553), respectively. All the diffraction peaks were compatible with the standard patterns of face-centered cubic spinel crystal structure with a space group of *Fd3m* (ZnV₂O₄, ICSD# 9009795; Co₂VO₄, JCPDS # 73-1633) [20–23]. The corresponding spinel crystal structure is shown in Figure 1c.

The thermogravimetric analysis was performed to predict the thermal stability of the resultant products, and the results are shown in Figure S1 (Supplementary Materials). The temperature increased from 35 to 800 °C at a heating rate of 5 °C/min in air to monitor the weight loss of the CVO/rGO composite. An increase in the weight with increasing temperature due to the oxidation of the CoV₂O₄ material under air could be seen. The weight changes could be classified into the following stages as: (i) the weight loss was about 1%, which occurred between 35–150 °C, and it was speculated that the moisture in the sample was removed; (ii) a 10% of weight increase at a temperature between 150 and 500 °C was observed, which was due to the oxidation reaction of CoO to Co₃O₄; and (iii) a final weight increase could be seen at the stage of ~500–650 °C, which was ascribed to the oxidation reaction of V₂O₃ to V₂O₅. In the range of 350 to 600 °C, the oxidation of carbon occurred [24]. However, the rGO oxidation shielded the further oxidation reaction of V–O matrix compounds during the air atmosphere test. Noticeably, more oxidation with weight increase was observed in the bare CVO sample. Moreover, the CVO/rGO sample showed a very small weight gain after 400 to 800 °C, resulting in the rGO modification promoting the thermal stability of the metal oxide material.

The morphology of the prepared samples was observed using microscopic techniques, namely SEM/TEM analysis. Figure 2a shows the SEM image of the bare CVO material, and it demonstrates the spherical size of the particles with an aggregated particle morphology. Figure 2b illustrates the CVO/rGO sample SEM image. An agglomerated particle morphology could be clearly seen, which was owed to the rGO covered from the CVO nanoparticles. In order to ensure the existence of CVO particles and rGO, we used TEM observation (Figure 2c,d). The prepared CVO particles exhibited two different sizes, namely nano-sized primary irregular particles and ultrasmall-sized secondary spherical particles (Figure 2c). Both as-prepared samples existed in a similar morphology of particles sizes. The primary particles size was in the range of 20 to 60 nm. Besides, the secondary particle size was found to be within 15 nm. The TEM image of the CVO/rGO sample is shown in Figure 2d, and the inset of Figure 2d displays the low magnification TEM image. Figure 2d demonstrates the fewer layers of graphene sheets obviously wrapping the CoV₂O₄ nanoparticles. The primary particles sizes were in the range of 15 to 30 nm and within 10 nm of the secondary particles. The addition of GO solution into the metal oxide mixture solution during the preparation may act as heterogeneous nucleation seeds to facilitate the formation of small crystal grains. Thus, the resultant CVO particles of the CVO/rGO sample showed a smaller size compared to the bare CVO sample. The nano sizes of the CVO particles would buffer the volume changes, and the rGO helped to

promote the electrical conductivity, as well as the electrical contact with the active particles during the sodiation/desodiation process.

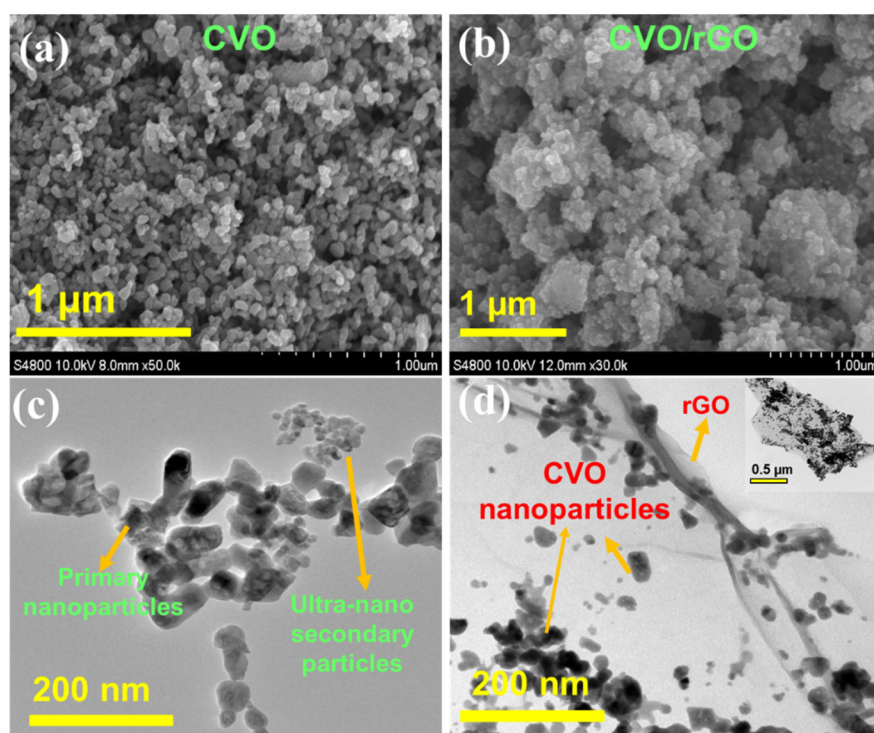


Figure 2. (a,b) SEM images and (c,d) TEM images of bare CoV_2O_4 and rGO-wrapped CoV_2O_4 materials (inset of Figure 2d is a large magnification TEM image of CVO/rGO sample).

The as-synthesized CVO material purity and its chemical elements oxidation states were analyzed by the X-ray photoelectron spectroscopy (XPS) and X-ray absorption spectroscopy (XAS) techniques. Figure 3a reveals the survey spectrum of the CVO sample, and the presence of Co, V, and O elements was confirmed. Figure 3b shows the Co 2p core spectra with Gaussian fitting, and it was distinguished into two different sets of binding energies. The major peak binding energies were found to be 781.4 and 798.9 eV and the satellite peaks binding energies around 787.2 and 803.3 eV, which were attributed to the Co 2p_{3/2} and Co 2p_{1/2} in 2+ oxidation state in the CVO material. The V2p narrow scan XPS result is shown in Figure 3c. The four deconvolution peaks of V existed in the 3+ and 5+ oxidation states. The V (3+) state peaks were located at 516.33 and 523.63 eV. The very small band peaks were exhibited around 517.05 and 524.88 eV, representing the V 5+ state. The spin-orbit splitting band difference was 7.3 and 7.8 eV for the 3+ and 5+ states. The values were close to earlier reports [17,18,20]. Furthermore, the oxidation state of V was verified by V K-edge X-ray absorption near edge structure spectroscopy (XANES) analysis. Figure S2 (Supplementary Materials) shows the V K-edge XANES result of the CVO material with the reference spectra of V, VO_2 , V_2O_3 , and V_2O_5 , respectively. The first absorption feature between 5465 and 5475 eV was ascribed to the pre-edge peak owing to the transition of the 1s core level to the 3d states. It was a dipole-prohibited transition, but initiated by the combination of strong 3d–4p mixing and the node of the metal 3d orbitals with the surrounding O 2p orbitals [25]. The lesser intensity of pre-edge peak was ascribed to the more symmetric VO_6 octahedra in the substituted compounds [26]. The spectra region around 5498.91 eV was similar to the V_2O_3 reference peak, which indicated V in the 3+ state. The small band regions were located at 5540.49 and 5567.31 eV, corresponding to V in 5+. Hence, the presence of mixed V 3+ and 5+ was confirmed in the CoV_2O_4 materials. Thus, the results of XPS and XAS indicated that the prepared materials exhibited the spin-glass behavior of V in the CVO spinel structure. The functional oxygen groups were analyzed from the core spectra of O 1s, and the result is shown in Figure 3d. The binding energies were located

at 530.3 and 531.6 eV, corresponding to the lattice oxygen of the oxygen metal framework (V–O–V) and the hydroxyl group from the moisture absorption on the surface of the sample.

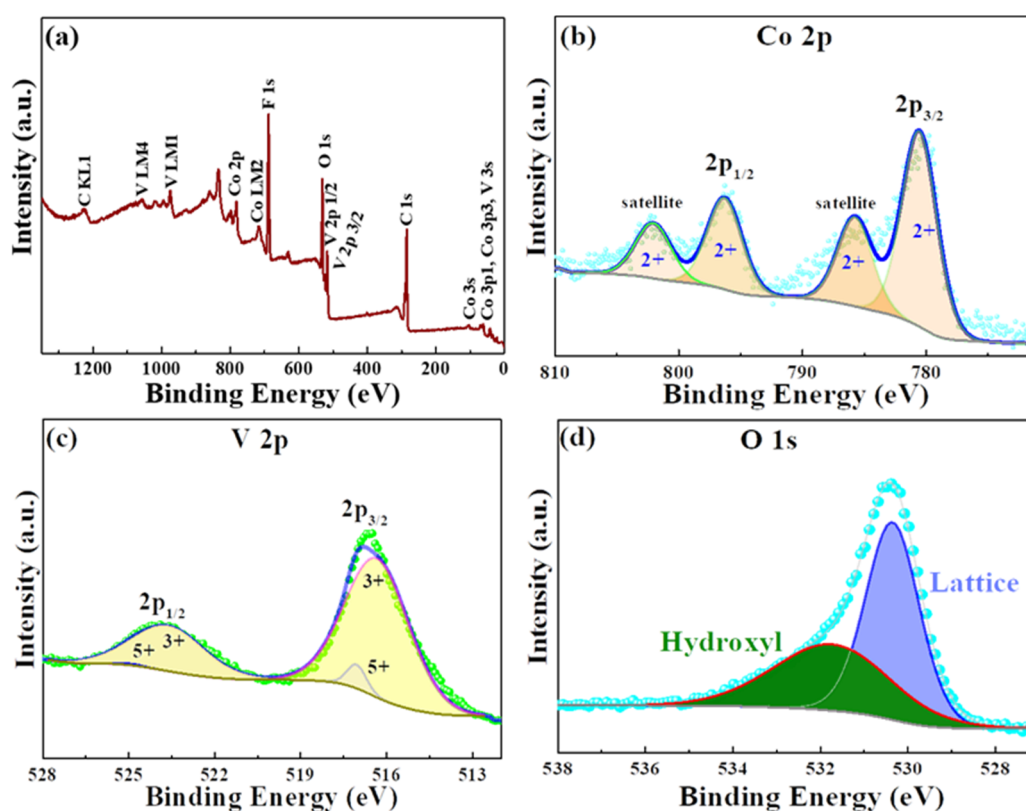


Figure 3. XPS spectra of the CoV_2O_4 sample: (a) wide range spectra; (b) Co 2p core spectra; (c) V2p core spectra; and (d) O1s core spectra.

Figure 4a shows the N_2 adsorption and desorption curves of bare CoV_2O_4 and rGO-wrapped CVO nanocomposite materials. The specific surface area was found to be $27 \text{ m}^2 \text{ g}^{-1}$ for CVO and $35 \text{ m}^2 \text{ g}^{-1}$ for CVO/rGO samples. The observed surface area was higher than that of some other metal oxide materials [27]. Figure 4b displays the pore volume distribution of the prepared bare CoV_2O_4 and CVO/rGO nanocomposite materials. A higher pore volume distribution was observed for the CVO/rGO sample ($0.2115 \text{ cm}^3/\text{g}$) compared with bare CVO ($0.1569 \text{ cm}^3/\text{g}$), which was presumably CoV_2O_4 particles no longer agglomerating into spheres, so the pore volume increased. The pore sizes of the materials were found to be 23.30 and 24.41 nm for bare CVO and CVO/rGO samples, indicating the mesoporous nature. The higher surface area and pore volume promoted the contact area between the material and the electrolyte and provided sufficient space to shield the volume expansion during the electrochemical reaction [28].

The electrochemical performances of the as-prepared materials were evaluated as an anode material for SIBs. The first, second, and third sodiation/desodiation profiles of CVO and rGO-wrapped CVO/Na cells are shown in Figure 5a,b at a current density of 100 mA g^{-1} , respectively. The discharge/charge platforms became similar in shape; however, the CVO/rGO electrode showed a higher reversible specific capacity. The bare CVO's reversible discharge capacity was 125 mAh g^{-1} , and the initial Coulombic efficiency was found to be 51% (Figure 5a). In addition, the enhancement of reversible discharge capacity was predicted for the CVO/rGO electrode cell. It was found to have a second cycle discharge capacity of 150 mAh g^{-1} and an initial Coulombic efficiency of 48% (Figure 5b).

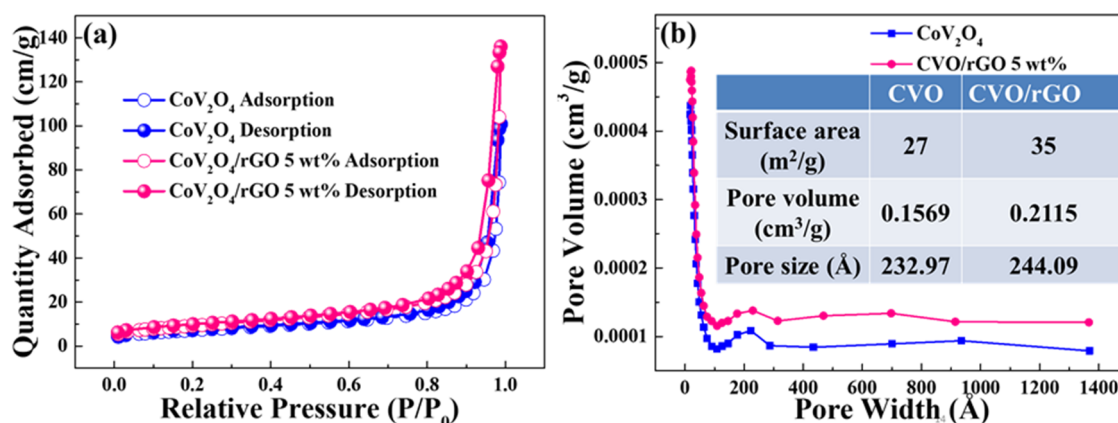


Figure 4. (a) Nitrogen adsorption isotherms and (b) the BJH desorption pore volume distributions of bare CoV_2O_4 and rGO-wrapped CoV_2O_4 materials; inset: the table shows the estimated values.

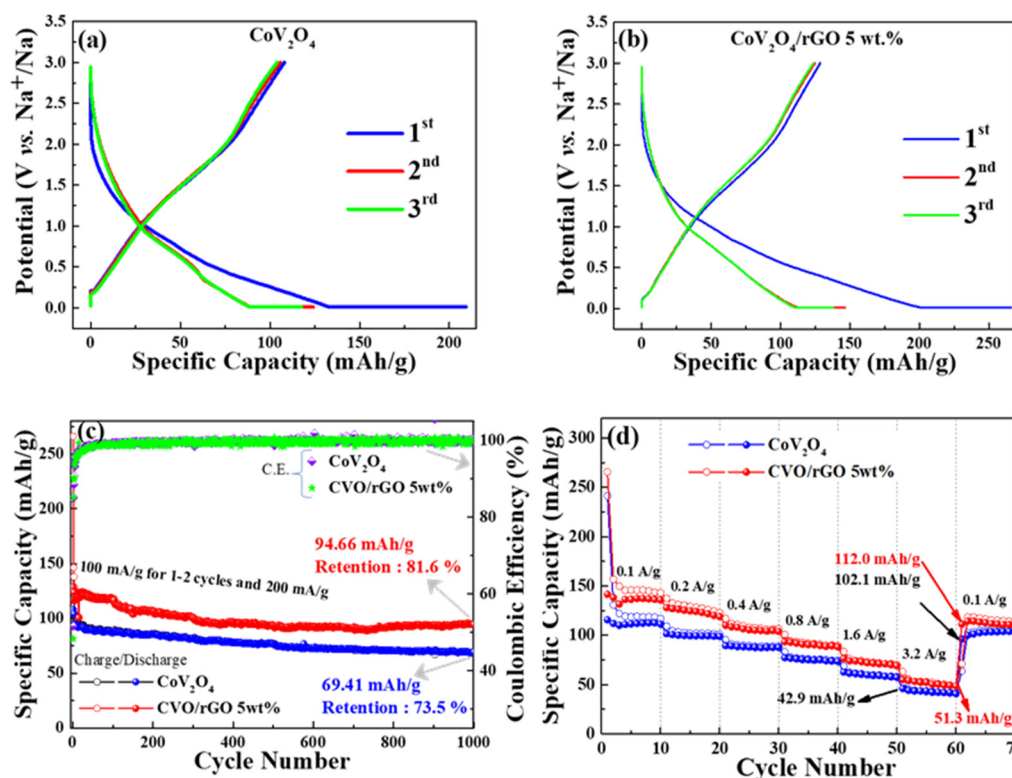


Figure 5. Electrochemical performance of Na ion storage: (a,b) discharge/charge profile of bare CoV_2O_4 and rGO-wrapped CoV_2O_4 electrodes; (c,d) cyclic stability and rate capability of bare CoV_2O_4 and rGO-wrapped CoV_2O_4 electrodes.

Figure 5c displays the cyclic stability test of both prepared samples. Initially, 1–3 cycles were performed at a current density of 100 mA g^{-1} , and subsequent cycles were carried out at 200 mA g^{-1} . The CVO/rGO electrode cell demonstrated higher capacity with cyclic stability than the bare CVO electrode, which was owed to the improvement of the conductivity of the bare materials. The Coulombic efficiency increased after the initial formation cycles and maintained around 98% over the 1000 cycles of both samples. The initial lower Coulombic efficiency was ascribed to the common issues of metal oxide anode materials due to the decomposition of the electrode active material under the phase conversion reaction during the sodiation process and the formation of the solid-electrolyte interface (SEI) film formation [29,30]. Furthermore, the higher surface area sample (CVO/rGO) hindered the initial Coulombic efficiency more than the bare material because of the side reaction on the electrolyte

and electrode. The CVO/rGO cell showed a discharge capacity of 94.66 mAh g⁻¹ over the 1000 cycles with a retention of 81.6% at 200 mA g⁻¹. The bare CVO electrode cell exhibited a discharge capacity of 69.41 mAh g⁻¹ with a retention of 73.5 % over the 1000 cycles at 200 mA g⁻¹. The observed reversible capacity of the CVO/rGO material illustrated higher performance than those of earlier reports of other oxide-based anode materials for SIBs [31,32]. The following reasons could be given for the remarkable cyclic stability of the prepared electrode materials: (i) the ultrasmall CVO nanoparticles shortened the Na⁺ ion diffusion distance; (ii) the appreciable surface area and porous nature with the combination of conductivity-based polymer binder possessed an electrochemically active thin stable layer of SEI, which may have improved the structural stability by acting as a buffer layer for the volume changes during the Na ion insertion and extraction processes [33–35]; (iii) the quantity of the total number of atoms that were close or on the surface was augmented when the particle size was reduced [36]; consequently, the accessible electroactive surface area was increased, resulting in improved electrochemical reaction; and (iv) the rGO additionally promoted the excellent electrical conductivity and the flexible higher surface area. Thus, the results showed this to have higher electrochemical stability and capacity as anode materials for SIB's. The high-rate Na ion storage capability test was performed at different current densities of 0.1, 0.2, 0.4, 0.8, 1.6, and 3.2 A g⁻¹, and the result is shown in Figure 5d. The prepared materials were fine candidates for high-rate sodium ion batteries. The CVO/rGO electrode delivered average specific capacities of 149, 127, 120, 99, 77, and 54 mAh g⁻¹ at current densities of 0.1, 0.2, 0.4, 0.8, 1.6, and 3.2 A g⁻¹, respectively. When the current density returned to 0.1 A g⁻¹, the electrode exhibited an average capacity of 114 mAh g⁻¹, revealing an appreciable high-rate capability.

The electrochemical kinetic behavior of the electrode cell was evaluated by the electrochemical impedance spectra (EIS) technique after five cycles at 100 mA g⁻¹. Both as-prepared electrode cells' Nyquist plots derived from EIS are shown in Figure 6a. The data were fitted by an equivalent circuit (see Figure 6a, inset), and the resultant fitting parameters are exposed in Table 1. The corresponding charge transfer resistance R_{ct} values of CVO/rGO and bare CVO were 17 and 86 Ω. The abundantly lower resistance of the CVO/rGO cell extremely promoted the transfer of electrons and Na ions during sodiation/desodiation reactions [17,18,20]. The diffusion coefficient of sodium ions can be calculated from the following equation:

$$D = (R^2 T^2) / (2 A^2 n^4 F^4 C^2 \sigma^2) \quad (1)$$

where R is the gas constant, T is the absolute temperature, A represents the electrode area, n is the number of electrons during charge/discharge, F is the Faraday constant, C is the concentration of sodium ions, and σ is the Warburg factor. The Warburg factor ($\sigma = Z'/\omega^{-1/2}$) can be explained by the diffusion barrier layer's impedance and semi-infinite diffusion impedance in the lower frequency slope after the semicircle. The σ was inversely proportional to the diffusion coefficient of Na⁺ [10]. Hence, the R_{ct} and σ were ascribed to the kinetic reaction of the cell. Figure 6b shows the CVO and CVO/rGO cells' linear fitting relationship plot between Z_{re} and the reciprocal square root of the lower angular frequencies. The slope values of the CVO and CVO/rGO electrodes were 5.81 and 2.55, respectively. The diffusion coefficients of Na ions could be estimated according to the above formula, which were 2.77 × 10⁻¹¹ and 1.44 × 10⁻¹⁰ cm² s⁻¹, respectively. The CVO/rGO cell demonstrated higher diffusivity than that of bare CVO, which meant it boosted the conductivity of the electrode. Thus, the CVO/rGO anode demonstrated finer capacity and rate capability. Besides, this material's electrochemical performance was lower than that of Li ion battery anodes [20]. To understand the reason, the electrochemical reaction mechanism was described via CV and ex situ XRD analysis.

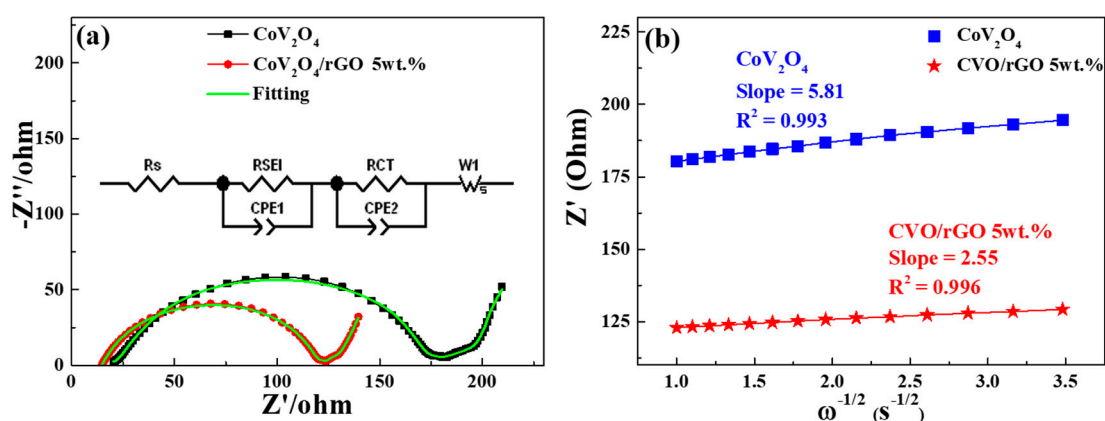


Figure 6. (a) Electrochemical impedance spectra (Nyquist plots); inset: the equivalent circuit used to fit the EIS; and (b) the liner fit of the relationship between Z' and $\omega^{-1/2}$ at low frequencies of the bare CoV_2O_4 and rGO-wrapped CoV_2O_4 electrodes.

Table 1. Impedance parameters and diffusion coefficients of the equivalent circuit.

Parameters	CoV_2O_4	CVO/rGO 5 wt. %
R_S (Ω)	10.54	14.32
R_{SEI} (Ω)	137.20	102.80
CPE1-T	1.2746×10^{-5}	2.0206×10^{-5}
CPE1-P	0.86534	0.83426
CPE2-T	0.015158	0.06819
CPE2-P	0.13263	0.24671
W1-R	96.72	162.3
W1-T	50.87	149.8
W1-P	0.67235	0.7404
R_{CT} (Ω)	86.20	17.10
Slope	5.81	2.55
R^2	0.993	0.996
Diffusion Coefficient (cm^2/s)	2.77×10^{-11}	1.44×10^{-10}

Figure 7a exhibits CV curves of the CVO electrode cell for the initial three cycles at a scan rate of 0.5 mV s^{-1} . The cathodic peaks at 1.1 V and 0.4–0.7 V were attributed to the Na ion insertion into CoV_2O_4 and conversion reaction that occurred to form CoO, as well as further reduction of CoO to Co [20,37]. The absence of the reduction band around 0.4 V after the first cycle represented the irreversible formation of SEI film. The broad band of the anodic peak was observed around 1.0 to 2.1 V, which was ascribed to Na ion extraction from the V–O matrix and the oxidation reaction from Co to CoO. The first cycle's cathodic current was reduced, and the second and third cycles' peaks were different than the first cycle. This represented the irreversible reaction of the first sodiation process. For the second and third cycles, the cathodic peak of 1.1 V was shifted to a lower voltage range, and reduction of CoO shifted to a higher voltage range, which was owed to the structural rearrangement in the initial charge process [38]. This showed that the CV curves at the second and third cycles almost overlapped, signifying the excellent electrochemical stability of the material.

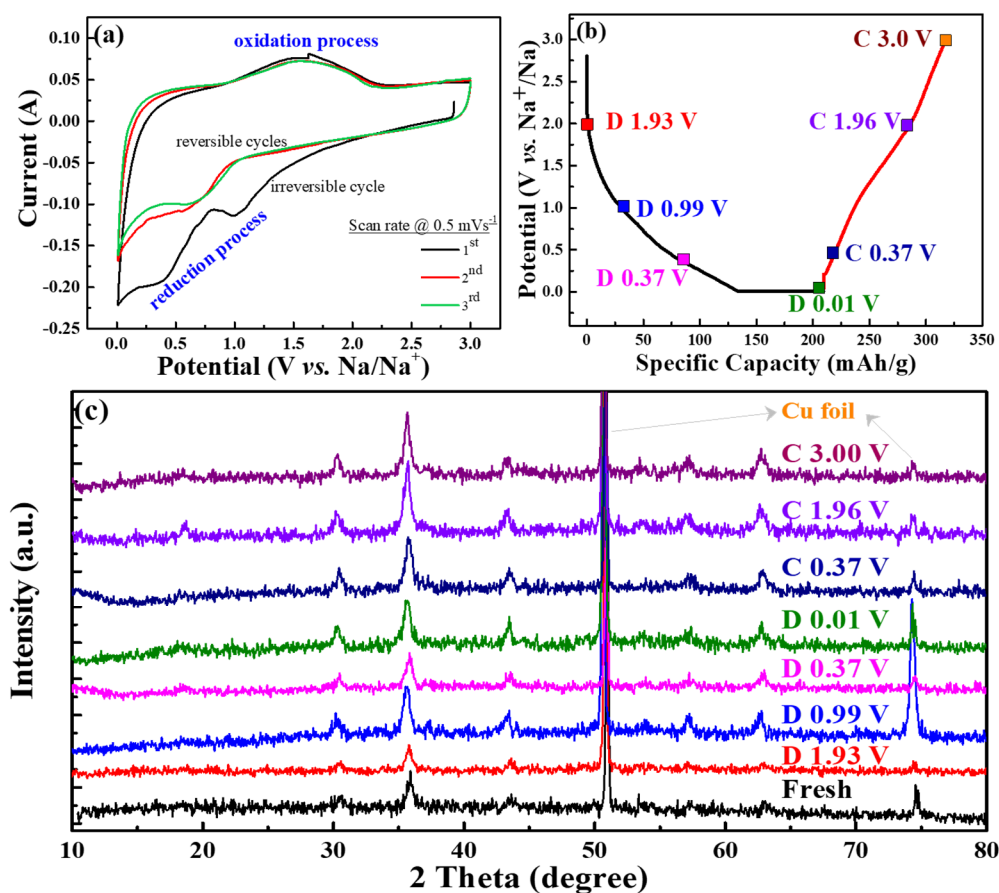


Figure 7. Sodiation/desodiation mechanism analysis of the CoV_2O_4 material electrode cell: (a) cyclic voltammetry (CV) curves in the potential window range of 0.01–3.0 V at a scan rate of 0.5 mV s^{-1} ; (b) discharge/charge profile at various voltage states for ex situ studies; and (c) ex situ XRD analysis.

Figure 7b displays different cut-off voltage states of the galvanostatic discharge/charge curves for the analysis of the ex situ XRD test at the first cycle, and Figure 7c shows the corresponding ex situ XRD patterns of the CVO sample at different charge/discharge states in the first cycle. The nature of the spinel structure was observed in the fresh electrode. The electrodes were adapted to the sodiation/desodiation process at various cut-off voltage ranges. Remarkably, the diffraction peaks of the CVO electrodes showed similar XRD patterns compared to that of fresh electrode, which suggested the incomplete electrochemical reaction. The Co standard X-ray diffraction peaks (ICSD # 44989, space group of Fm-3m) of 2θ values were 44.37° (111), 51.59° (200), and 75.92° (220), respectively. The standard pattern of CoO (ICSD # 29082, space group: F-43m) exhibited 34.17° (111), 39.66° (200), 57.24° (220), 68.39° (311), and 71.84° (222), respectively. Obviously, the diffraction peaks of Co were similar to fresh electrodes, and they were difficult to distinguish. However, the diffraction peaks of the fresh electrode slightly shifted to a lower angle during the sodiation/desodiation process (Figure S3 in Supplementary Materials). At a discharge of 0.01 V, very small characteristic peaks appeared at the position of 44.5° . It was thought that the partial conversion reaction of CVO was observed during the first sodiation cycle. This phenomenon implied the confirmation of the insertion/extraction of Na^+ during the discharge/charge process. Hence, the electrochemical performance showed lower capacities compared to the conversion reaction of Li ion storage [20]. In addition, the deficient electrochemical performance might have been the Na_2O or 2NaVO_2 formation during the sodiation/desodiation process [39]. The Na_2O or $\text{NaVO}_2(\text{O}_3)$ phases acted as an ionic, as well as electronic insulator and prevented further conversion reaction into CVO material [39,40]. Overall, the as-synthesized rGO-wrapped CVO material showed a remarkable enhancement of the electrochemical performance, and the following factors

could be described: (i) the rGO with complete coverage of CoV_2O_4 nanoparticles provided adequate electrode-electrolyte contact areas for more Na^+ ion transfer across the interface and shortened the length of Na^+ ion diffusion; (ii) the rGO aided efficiently accommodating the volume change during the sodiation/desodiation process; and (iii) the rGO-modified CVO improved the conductivity.

4. Conclusions

We successfully synthesized the rGO-wrapped CoV_2O_4 nanocomposite by the solvothermal technique. The cubic spinel crystal structure was revealed. The CVO/rGO sample had a specific surface area of $35 \text{ m}^2/\text{g}$, and it was comparably higher than that of bare CVO ($27 \text{ m}^2/\text{g}$). The as-synthesized materials were both applied to sodium ion storage anodes for the first time. The results showed excellent long-term cyclic stability and good rate performance. The rGO-wrapped CoV_2O_4 electrode cell exhibited a higher reversible discharge capacity of 150 mAh g^{-1} and retained 81.6% of capacity after 1000 cycles at 200 mA g^{-1} . For the rate performance, it demonstrated a capacity of 54 mAh g^{-1} at 3200 mA g^{-1} . Moreover, the bare CVO electrode cell obtained 73.5 % of retention after 1000 cycles at 200 mA g^{-1} . The discharge capacity was found to be 43 mAh g^{-1} at the current density of 3200 mA g^{-1} . Normally, the Na ion insertion/extraction process in metal oxide-based anodes causes large volume changes, leading to the pulverization process and a loss of electrical contact. Consequently, in this work, the rGO sheets wrapped with CVO nanoparticles served as a highly conductive framework to sustain the electrical contact from the CVO nanoparticles to the current collectors and improved the capacity and cycling stability due to their high electrical conductivity and large surface area. This work opens a prospect to develop this potential candidate for vanadium-based metal oxide anode materials for high performance SIB applications.

Supplementary Materials: The following are available online at <http://www.mdpi.com/2073-4360/12/3/555/s1>, Figure S1: TGA analysis of synthesized bare CoV_2O_4 and rGO-wrapped CoV_2O_4 materials; Figure S2: V K-edge X-ray absorption near edge structure spectroscopy (XANES) of CoV_2O_4 powder and the references of V, VO_2 , V_2O_3 , and V_2O_5 spectra; Figure S3: Enlarge 2 values of *ex-situ* XRD analysis of CVO electrode cells.

Author Contributions: R.M. wrote the paper with a contribution to the experiments and analysis; J.-S.L. contributed to the experiments and analysis; W.-R.L. supervised and edited the manuscript. All authors read and agreed to the published version of the manuscript.

Funding: The authors gratefully acknowledge the Ministry of Science and Technology, Taiwan, for the project grants 107-2811-M-033-506, 108EFD0500003, 108-2811-E-033-500, 109-2911-I-033-502, 108-E-033-MY3, and 109-3116-F-006-018.

Conflicts of Interest: The authors declare no conflict of interest.

References

1. Xu, X.; Xiong, F.; Meng, J.; Wang, X.; Niu, C.; An, Q.; Mai, L. Vanadium-Based Nanomaterials: A Promising Family for Emerging Metal-Ion Batteries. *Adv. Funct. Mater.* **2020**, 1904398. [CrossRef]
2. Fang, Y.; Yu, X.-Y.; Lou, X.W. Nanostructured Electrode Materials for Advanced Sodium-Ion Batteries. *Matter* **2019**, *1*, 90–114. [CrossRef]
3. Liu, P.; Zhu, K.; Gao, Y.; Luo, H.; Lu, L. Recent Progress in the Applications of Vanadium-Based Oxides on Energy Storage: From Low-Dimensional Nanomaterials Synthesis to 3D Micro/Nano-Structures and Free-Standing Electrodes Fabrication. *Adv. Energy Mater.* **2017**, *7*, 1700547. [CrossRef]
4. Fang, S.; Bresser, D.; Passerini, S. Transition Metal Oxide Anodes for Electrochemical Energy Storage in Lithium- and Sodium-Ion Batteries. *Adv. Energy Mater.* **2020**, *10*, 1902485. [CrossRef]
5. Luo, M.; Yu, H.; Hu, F.; Liu, T.; Cheng, X.; Zheng, R.; Bai, Y.; Shui, M.; Shu, J. Metal selenides for high performance sodium ion batteries. *Chem. Eng. J.* **2020**, *380*, 1225572. [CrossRef]
6. Chen, J.; Chua, D.H.C.; Lee, P.S. The Advances of Metal Sulfides and In Situ Characterization Methods beyond Li Ion Batteries: Sodium, Potassium, and Aluminum Ion Batteries. *Small Methods* **2020**, *4*, 1900648. [CrossRef]
7. Tan, H.; Feng, Y.; Rui, X.; Yu, Y.; Huang, S. Metal Chalcogenides: Paving the Way for High Performance Sodium/Potassium-Ion Batteries. *Small Methods* **2020**, *4*, 1900563. [CrossRef]

8. Yuan, C.; Wu, H.B.; Xie, Y.; Lou, X.W. Mixed Transition-Metal Oxides: Design, Synthesis, and Energy-Related Applications. *Angew. Chem. Int. Ed.* **2014**, *53*, 1488–1504. [[CrossRef](#)]
9. Ni, S.; Liu, J.; Chao, D.; Mai, L. Vanadate-Based Materials for Li-Ion Batteries: The Search for Anodes for Practical Applications. *Adv. Energy Mater.* **2019**, *9*, 1803324. [[CrossRef](#)]
10. Muruganantham, R.; Liu, W.R.; Lin, C.H.; Rudysh, M.; Piasecki, M. Design of meso/macro porous 2D Mn-vanadate as potential novel anode materials for sodium ion storage. *J. Energy Storage* **2019**, *26*, 100915. [[CrossRef](#)]
11. Qin, Z.; Lv, C.; Pei, J.; Yan, C.; Hu, Y.; Chen, G. A 1D Honeycomb-Like Amorphous Zincic Vanadate for Stable and Fast Sodium-Ion Storage. *Small* **2020**, *16*, 1906214. [[CrossRef](#)] [[PubMed](#)]
12. Wang, Y.-X.; Chou, S.-L.; Liu, H.-K.; Dou, S.-X. Reduced graphene oxide with superior cycling stability and rate capability for sodium storage. *Carbon* **2013**, *57*, 202–208. [[CrossRef](#)]
13. Wen, Y.; He, K.; Zhu, Y.; Han, F.; Xu, Y.; Matsuda, I.; Ishii, Y.; Cumings, J.; Wang, C. Expanded graphite as superior anode for sodium ion batteries. *Nat. Commun.* **2014**, *5*, 4033. [[CrossRef](#)]
14. Kumar, N.A.; Gaddam, R.R.; Varanasi, S.R.; Yang, D.; Bhatia, S.K.; Zhao, X.S. Sodium ion storage in reduced graphene oxide. *Electrochim. Acta* **2016**, *214*, 319–325. [[CrossRef](#)]
15. Wu, F.; Wang, X.; Li, M.; Xu, H. A high capacity NiFe₂O₄/RGO nanocomposites as superior anode materials for sodium ion batteries. *Ceram. Int.* **2016**, *42*, 16666–16670. [[CrossRef](#)]
16. Sekhar, B.C.; Packiyalakshmi, P.; Kalaiselvi, N. Custom designed ZnMn₂O₄/nitrogen doped graphene composite anode validated for sodium ion battery application. *RSC Adv.* **2017**, *7*, 20057–20061. [[CrossRef](#)]
17. Zhang, D.; Li, G.; Li, B.; Fan, J.; Chen, D.; Liu, X.; Li, L. Fast synthesis of Co_{1.8}V_{1.2}O₄/rGO as a high-rate anode material for lithium ion batteries. *Chem. Commun.* **2018**, *54*, 7689–7692. [[CrossRef](#)]
18. Zhang, D.; Xi, S.; Li, G.; Li, B.; Fan, J.; Liu, X.; Chen, D.; Li, L. Facile synthesis of Mn_{2.1}V_{0.9}O₄/rGO: A novel high-rate anode material for lithium ion batteries. *J. Power Sources* **2019**, *426*, 197–204. [[CrossRef](#)]
19. Li, Y.; Zhao, Y.; Ma, C.; Shi, J.; Zhao, Y. Highly monodispersed graphene/SnO₂ hybrid nanosheets as bifunctional anode materials of Li ion and Na ion batteries. *J. Alloys Compd.* **2020**, *821*, 153506. [[CrossRef](#)]
20. Lu, J.-S.; Maggay, I.V.B.; Liu, W.-R. CoV₂O₄: A novel anode material for lithium ion batteries with excellent electrochemical performance. *Chem. Commun.* **2018**, *54*, 3094–3097. [[CrossRef](#)]
21. Xiao, L.; Zhao, Y.; Yin, J.; Zhang, L. Clewlike ZnV₂O₄ Hollow Spheres: Nonaqueous Sol-Gel Synthesis, Formation Mechanism, and Lithium Storage Properties. *Chem. Eur. J.* **2009**, *15*, 9442–9450. [[CrossRef](#)] [[PubMed](#)]
22. Gutierrez, A.; Manthiram, A. Microwave-Assisted Solvothermal Synthesis of Spinel AV₂O₄ (M = Mg, Mn, Fe, and Co). *Inorg. Chem.* **2014**, *53*, 8570–8576. [[CrossRef](#)] [[PubMed](#)]
23. Muruganantham, R.; Maggay, I.V.B.; Juan, L.M.Z.D.; Nguyen, M.T.; Yonezawa, T.; Lin, C.-H.; Lin, Y.-G.; Liu, W.-R. Electrochemical exploration of the effects of calcination temperature of a mesoporous zinc vanadate anode material on the performance of Na ion batteries. *Inorg. Chem. Front.* **2019**, *6*, 2653–2659. [[CrossRef](#)]
24. Palanisamy, K.; Um, J.H.; Jeong, M.; Yoon, W.-S. Porous V₂O₅/RGO/CNT hierarchical architecture as a cathode material: Emphasis on the contribution of surface lithium storage. *Sci. Rep.* **2016**, *6*, 31275. [[CrossRef](#)]
25. Sharma, A.; Varshney, M.; Chae, K.-H.; Won, S.O. Electronic structure and luminescence assets in white-light emitting Ca₂V₂O₇, Sr₂V₂O₇ and Ba₂V₂O₇ pyro-vanadates: X-ray absorption spectroscopy investigations. *RSC Adv.* **2018**, *8*, 26423–26431. [[CrossRef](#)]
26. Wen, B.; Wang, Q.; Lin, Y.; Chernova, N.A.; Karki, K.; Chung, Y.; Omenya, F.; Sallis, S.; Piper, L.F.J.; Ong, S.P.; et al. Molybdenum Substituted Vanadyl Phosphate ε-VOPO₄ with Enhanced Two-Electron Transfer Reversibility and Kinetics for Lithium-Ion Batteries. *Chem. Mater.* **2016**, *28*, 3159–3170. [[CrossRef](#)]
27. Moorhead-Rosenberg, Z.; Harrison, K.L.; Turner, T.; Manthiram, A. A Rapid Microwave-Assisted Solvothermal Approach to Lower-Valent Transition Metal Oxides. *Inorg. Chem.* **2013**, *52*, 13087–13093. [[CrossRef](#)]
28. Seok, D.; Jeong, Y.; Han, K.; Yoon, D.Y.; Sohn, H. Recent Progress of Electrochemical Energy Devices: Metal Oxide–Carbon Nanocomposites as Materials for Next-Generation Chemical Storage for Renewable Energy. *Sustainability* **2019**, *11*, 3694. [[CrossRef](#)]
29. Ma, Y.; Wang, Q.; Liu, L.; Yao, S.; Wu, W.; Wang, Z.; Lv, P.; Zheng, J.; Yu, K.; Wei, W.; et al. Plasma-Enabled Ternary SnO₂@Sn/Nitrogen-Doped Graphene Aerogel Anode for Sodium-Ion Batteries. *ChemElectroChem.* **2020**, *7*. [[CrossRef](#)]

30. Zhang, S.; Li, X.; Ding, B.; Li, H.; Liu, X.; Xu, Q. A novel spitball-like $\text{Co}_3(\text{NO}_3)_2(\text{OH})_4@Zr\text{-MOF}@RGO$ anode material for sodium ion storage. *J. Alloys Compd.* **2020**, *822*, 153624. [[CrossRef](#)]
31. Kim, H.; Kim, D.Y.; Kim, Y.; Lee, S.-S.; Park, K. Na Insertion Mechanisms in Vanadium Oxide Nanotubes for Na-Ion Batteries. *ACS Appl. Mater. Interfaces* **2015**, *7*, 1477–1485. [[CrossRef](#)]
32. Wu, D.; Li, X.; Xu, B.; Twu, N.; Liu, L.; Ceder, G. NaTiO_2 : A layered anode material for sodium ion batteries. *Energy Environ. Sci.* **2015**, *8*, 195–202. [[CrossRef](#)]
33. Li, T.; Li, X.; Wang, Z.; Guo, H.; Li, Y. A novel NiCo_2O_4 anode morphology for lithium ion batteries. *J. Mater. Chem. A* **2015**, *3*, 11970–11975. [[CrossRef](#)]
34. Lee, B.; Paek, E.; Mitlin, D.; Lee, S.W. Sodium Metal Anodes: Emerging Solutions to Dendrite Growth. *Chem. Rev.* **2019**, *119*, 5416–5460. [[CrossRef](#)]
35. Zhao, Y.; Adair, K.; Sun, X. Recent developments and insights into the understanding of Na metal anodes for Na-metal batteries. *Energy Environ. Sci.* **2018**, *11*, 2673–2695. [[CrossRef](#)]
36. Lu, L.; Wang, J.-Z.; Zhu, X.-B.; Gao, X.-W.; Liu, H.-K. High capacity and high rate capability of nanostructured CuFeO_2 anode materials for lithium ion batteries. *J. Power Sources* **2011**, *196*, 7025–7029. [[CrossRef](#)]
37. Chang, L.; Wang, K.; Huang, L.; He, Z.; Shao, H.; Wang, J. Hierarchically porous CoO microsphere films with enhanced lithium/sodium storage properties. *J. Alloys Compd.* **2017**, *725*, 824–834. [[CrossRef](#)]
38. Zhou, X.; Zhong, Y.; Yang, M.; Zhang, Q.; Wei, J.; Zhou, Z. $\text{Co}_2(\text{OH})_2\text{CO}_3$ Nanosheets and CoO Nanonets with Tailored Pore Sizes as Anodes for Lithium Ion Batteries. *ACS Appl. Mater. Interfaces* **2015**, *7*, 12022–12029. [[CrossRef](#)]
39. Dixon, D.; Ávila, M.; Ehrenberg, H.; Bhaskar, A. Difference in Electrochemical Mechanism of SnO_2 Conversion in Lithium-Ion and Sodium-Ion Batteries: Combined in Operando and Ex Situ XAS Investigations. *ACS Omega* **2019**, *4*, 9731–9738. [[CrossRef](#)]
40. Hamani, D.; Ati, M.; Tarascon, J.-M. Patrick Rozier, Na_xVO_2 as possible electrode for Na ion batteries. *Electrochem. Commun.* **2011**, *13*, 938–941. [[CrossRef](#)]



© 2020 by the authors. Licensee MDPI, Basel, Switzerland. This article is an open access article distributed under the terms and conditions of the Creative Commons Attribution (CC BY) license (<http://creativecommons.org/licenses/by/4.0/>).